Chapter 6

Spatiotemporal Self-Organization in Formic Acid Oxidation

6.1 Introduction

Ever since the early work by Ostwald [14] and Heathcote [179, 180] on the electrodissolution of cromium and iron, it is known that electrochemical processes do not necessarily proceed in a spatially homogeneous manner at the electrified interface. In recent years, interdisciplinary research conducted by electrochemists and non-linear dynamicists alike has made substantial advances in the understanding of such self-organized, non-equilibrium patterns in electrochemical systems [32, 23, 27].

In this chapter new spatiotemporal inhomogeneous potential patterns near the electrode interface are investigated. The question of sign, strength and range of the spatial coupling will thereby turn out to be the key for a sound understanding of the observations. Important stimuli for theses studies were drawn from theoretical predictions concerning the relation between electrode geometry and coupling in generalized electrochemical models [40].

The electrocatalytic oxidation of formic acid on Pt electrodes was chosen as the experimental system for the following reasons: (i) The temporal behavior has thoroughly been characterized both experimentally and theoretically (ii) the mechanistic origin of the bistable and oscillatory regime are well understood (iii) there have not been any investigations of an electrocatalytic oscillatory system belonging to the HNDR category and most importantly (iv) unlike other electrocatalytic systems both the cyclovoltammetric and the dynamical features of the FA oxidation are relatively insensitive to the mass transport conditions of the electroactive species easing the observation of potential distributions by means of local potential probes.

The chapter is organized as follows: After a short review on previous experimental work on electrochemical patterns, the experimental details concerning the setup and conditions are described (see also section 3.2.4.). Thereafter, the experimental findings are presented followed by a concluding discussion.

6.2 Previous Work

6.2.1 Metal dissolution

Spatial inhomogeneities with respect to the local reaction rate are well observable in electrodissolution processes, since the oxidation state of the electrode material is changed in layers of considerable thickness associated with changes in the optical properties of the electrode surface. This is why research on spatial patterns naturally focused first on anodic dissolution reactions of metals such as Fe, Co, Ni, Cr or Pb in acidic environments. In particular, the Fe dissolution system received much interest in the search for spatial patterns. While Franck and Bonhoeffer et al. [181, 13, 182] reported an activation front and wave propagation along Fe wires, Pigeau and Kirkpatrick [183] presented images where a passivation front emerged at the rim of a Fe-disk electrode and propagated towards the center. Later, Hudson [184] extended the search for patterns in these systems to other potential regions and found a radial symmetry breaking including spatiotemporal period-doubling bifurcations. Similarly, the Co dissolution system [87, 185, 186, 187] was also reported to exhibit activation/passivation fronts as well as complex wave modulations on both ring and disk electrodes.

An interesting experiment was performed by Lev et al. [34, 82] during anodic dissolution of long Ni wires in acidic media. They found anti-phase behavior of the local interfacial currents under galvanostatic control, i.e. a dynamical regime where at any time instant the local current along one half of the electrode wire was shifted by 180° relative to the other half.

6.2.2 Electrocatalytic reactions

Spatial patterns in electrocatalytic systems have only recently become the focus of electrochemists, as the spatial imaging, especially for disk electrodes, requires more sophisticated methods compared to dissolution systems [35].

Flätgen and Krischer [188] reported on wave phenomena in the oscillatory regime during peroxodisulphate reduction on a Ag disk electrode. An activation front emerged at the electrode rim spread across the entire electrode followed by a slow, almost homogeneous repassivation process.

In the bistable regime of the $S_2O_8^{2-}$ system [35, 84, 85] accelerating potential fronts along a Ag ring electrode during passive/active transitions were measured. The average front velocity was found to be dependent linearly on the conductivity in some concentration range and ranged between a few cm/s and m/s.

Finally, very recently the observation of decelerating and stationary fronts during active/passive transitions was reported in the bistable regime of the $S_2O_8^{2-}$ system on Ag ring electrodes, as a point-like reference electrode was approached towards the center of the ring electrode [189].

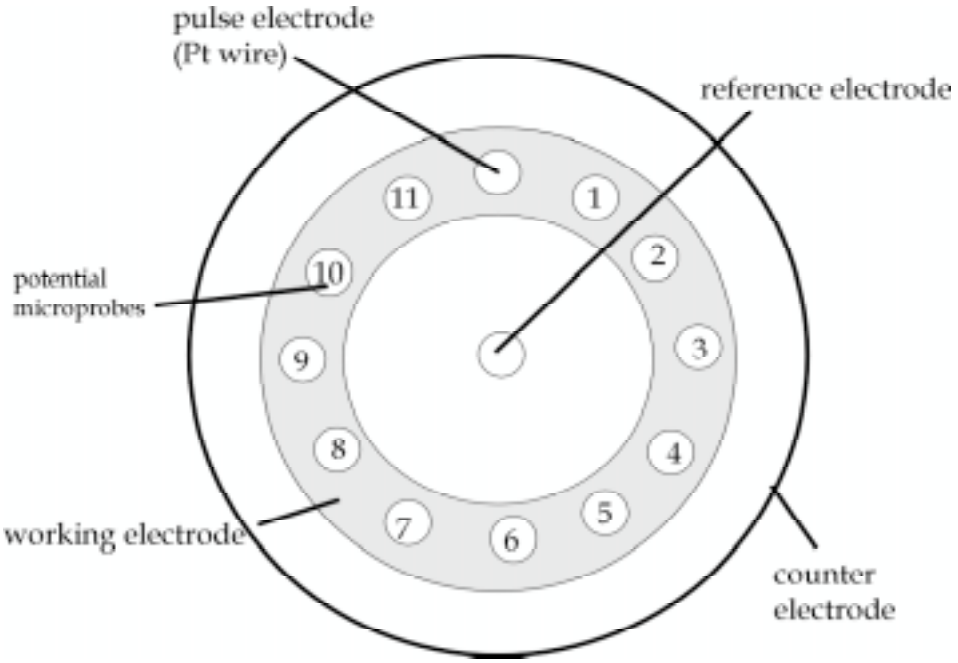

Figure 6-1: Top view of multi-electrode array setup. There is a 30 degree angle between adjacent microprobes except for electrodes 1 and 11 between which the pulse electrode is located. In upcoming figures the number of the potential probes will be associated with the respective spatial position along the ring.

6.3 Experimental

6.3.1 Setup

The principal three-electrode arrangement for the measurement of the local potential distribution near the electrochemical interface was discussed in section 3.2.4. Fig. 6-1 shows the top view of the multi-probe setup including the numbering of the potential probes as used in upcoming figures. The number of the local probe is to represent the spatial position along the working electrode (WE). Recall that the reference electrode (RE) was placed in the center of the WE ring.

In preliminary tests, only two local potential probes (associated with potentials ϕ_1 and ϕ_2) together with the pulse electrode were placed near the WE. Probes ϕ_1 and ϕ_2 were placed on opposite sides of the ring, while the pulse electrode was approached towards the WE in immediate vicinity to probe ϕ_1. This numbering will be used throughout all following two-probe measurements.

6.3.2 Experimental pretreatment, preparation and conditions

Prior to experiments the polycrystalline Pt ring electrode (WE) was chemically cleaned in Caroic acid for about 10 - 30 min. This solution is most efficient in

removing all organic surface deposits, however, sometimes introduces oxygen containing species into the electrode material as seen in the initial CVs. Therefore, in later experiments, only sulfuric acid (suprapure) was used as cleaning reagent. After rinsing using triply distilled water, the WE was subsequently mounted in the teflon lid of the cell which already held both the pulse electrode and the counter electrode. The lid was rapidly placed on the main chamber containing a mixture of $HCOONa$ (p.a.) and H_2SO_4 (suprapure). The solution concentrations used included $0,1\ M$: $0,05\ M$, $0,05\ M$: $0,025\ M$, $0,01\ M$: $0,005\ M$ for HCOONa : $H_2\ SO_4$, respectively. Table 6.1 summarizes some properties of the solutions used as calculated from known relations.

Next, the capillary potential probes were filled with a 0,5 M Na_2SO_4 solution, capped with a commercial Hg/Hg_2SO_4 reference electrode and mounted one by one into the teflon id. Finally, the RE (Hg/Hg_2SO_4) was placed in the central drill-whole followed by careful alignment of all capillary tips with respect to the WE ring. Subsequently, the electrochemical system was carefully deoxygenated using nitrogen.

6.3.3 Potential measurements

Outer potential U

Potential values regarding the WE refer to the central Hg/Hg_2SO_4 (+430 mV against SCE) with the exception of Fig. 6-2 where potentials refer to the SCE.

Local potentials

The potentials reported for the local potential probes were measured with respect to the WE potential and became subsequently inverted by the amplifier. Thus, the local potentials reported in the upcoming sections represent the local potential drops between WE and the respective location of the capillary tip inside the electrolyte. Assuming the ohmic potential drop across the remaining portion of the electrolyte between capillary tip and WE to be small compared to the interfacial drop (especially at low total currents), the local potentials provide a good approximation for the instantaneous local interfacial potential drops, i.e. the double layer potential ϕ_{dl} .

Perturbation Potentials

Perturbation potentials applied by means of the pulse (trigger) electrode are relative to the WE. In spite of the small distance between the pulse electrode and the WE, the perturbation had to be quite large (of the order of volts) in order to induce local transitions at the WE.

6.4 Results

6.4.1 The cyclovoltammetric profile and the operating points

Fig. 6-2 displays a typical I/U curve for the electrochemical cell used in the absence of an external ohmic resistance. On the anodic scan, Peak I, i.e. the direct FA oxida-

solution $HCOONa/H_2SO_4$	conductivity [1/Ω cm]	pH
0,1 M/0,05 M	10×10^{-3}	2,4
0,05 M/0,025 M	$5{,}6\times10^{-3}$	2,5
0,01 M/0,005 M	$1{,}3\times10^{-3}$	2,9

Table 6.1: electrolyte solutions used in experiments and calculated properties κ and pH ($\kappa = \sum_i z_i F u_i c_i$)

tion occurring on sites not blocked by CO in the absence of considerable amounts of oxygen-containing species, is visible as shoulder, followed by Peak II where CO becomes gradually removed giving way to high rate of direct FA oxidation (active state). At more anodic potentials a narrow potential range of spontaneous current oscillations appear preceded by small current wiggles. More anodically, oxygen-containing species poison the surface and deactivate the electrode. Upon turning the potential scan, the electrode remains deactivated (passive state). The system then enters the bistable regime (active and passive state coexisting) until at more cathodic potentials a sudden desorption of the poisoning species occurs which brings the system back on the active branch of the CV.

Forced transitions from active to the passive state, as described later, were performed near the peak potential of Peak II, while forced passive-active transitions were performed near the sharp desorption edge.

In experiments focusing on oscillatory behavior the outer potential was increased from low values (CO poisoning) to values on the cathodic flank of Peak II until spontaneous oscillations set in. Owing to impurities and partial premature deactivation of the electrode, it became necessary in some experiments to apply a small homogeneous potential perturbation on the WE in order to induce the oscillations.

6.4.2 Monitoring the local interfacial potential

Potential scans

Fig. 6-3 shows the total current vs. outer applied potential U during an anodic scan (10 mV/s). Clearly visible are Peak I and II. Also shown in the Fig. are the two local probe potential (amplified by factor 10) which show a linear increase as long as the total current I is low, followed by considerable deviation from a linear dependence when I rises. This behavior is in agreement with simple relation $U = \phi_{dl} + R_{sol} I$, assuming the probe potential to be a rough approximation of the interfacial potential.

The small delay in the local potentials on the anodic flank of Peak II indicates that small inhomogeneities in the potential distribution are induced by the finite scan rate in combination with imperfections of the cell symmetry and of the response of the WE.

This is drastically evidenced by the measurement given in Fig. 6-4 where the counter electrode was placed asymmetrically outside the WE ring near the local probe ϕ_1. For small currents the local potentials on opposite sides are shifted by some constant value. Upon oxygen-poisoning (sloppily used for the deposition of oxygen-containing poisons such as Pt-OH or/and Pt-O at more anodic potentials)

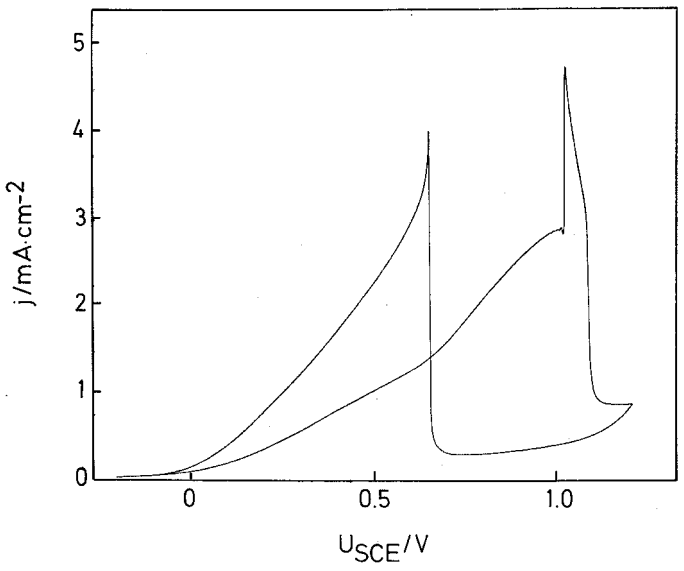

Figure 6-2: Cyclovoltammetric profile during formic acid oxidation on a poly-Pt ring electrode, 0.1 M HCOONa/ 0.05 M H_2SO_4, R= 0 Ω, scan rate 10 mV/s, no stirring.

first the local potential ϕ_1 rises indicating the poisoning of the neighboring electrode area, followed by the delayed oxygen-poisoning of the opposite side. This kind of inhomogeneity is clearly due to the geometrical conditions and must not be confused with spontaneously formed inhomogeneities at constant potentials U discussed in forthcoming sections.

Potential perturbations in the active state

In Fig. 6-5 the local response to a 100 ms positive potential perturbation is displayed as measured with the multi-probe setup (only probes 2 through 11 were used, concentrical counter electrode throughout). As a positive potential perturbation decreases the interfacial potential drop, the potential distribution falls off at the edges of the graphical surface (position near the pulse electrode). However, the local potential on the opposite side increases during the perturbation. Similarly, when applying a negative perturbation (Fig. 6-6) the interfacial potential drop rises near the pulse electrode, while it decreases on the opposite side

6.4.3 Travelling front patterns during the active-passive transition

As demonstrated in Fig. 6-2, the WE becomes quickly deactivated by surface poisons once the outer potential has reached a critical anodic value. The deactivation manifests itself most clearly in the sharp current drop on the anodic flank of Peak II. In

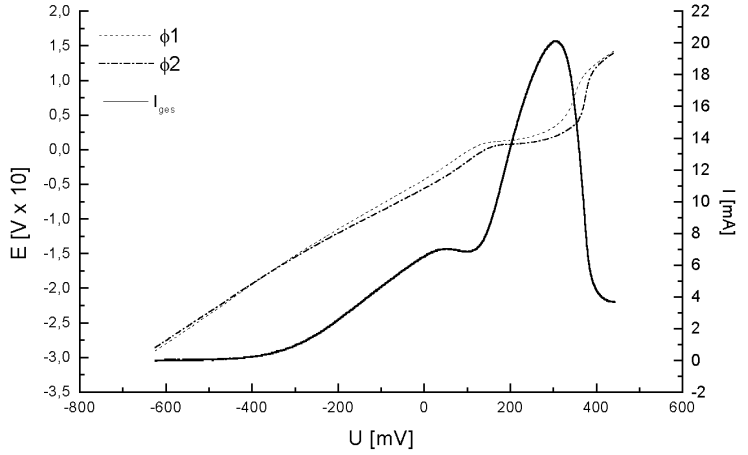

Figure 6-3: Voltammetric profile recorded during anodic scan for symmetric counter ring electrode (solid), parallel recording of local potentials ϕ_1 and ϕ_2 near the WE by means of potential probes on opposite sides, other conditions as in previous figure.

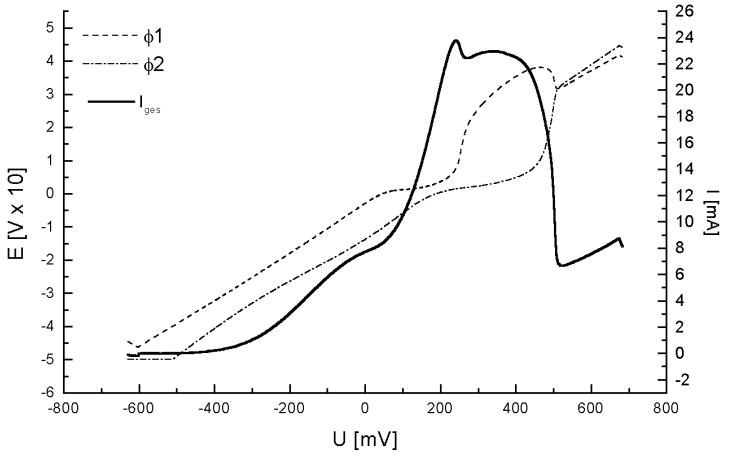

Figure 6-4: Voltammetric profile recorded during anodic scan for asymmetric counter electrode (solid), parallel recording of local potentials ϕ_1 and ϕ_2 near the WE by means of potential probes on opposite sides, conditions as in previous figure.

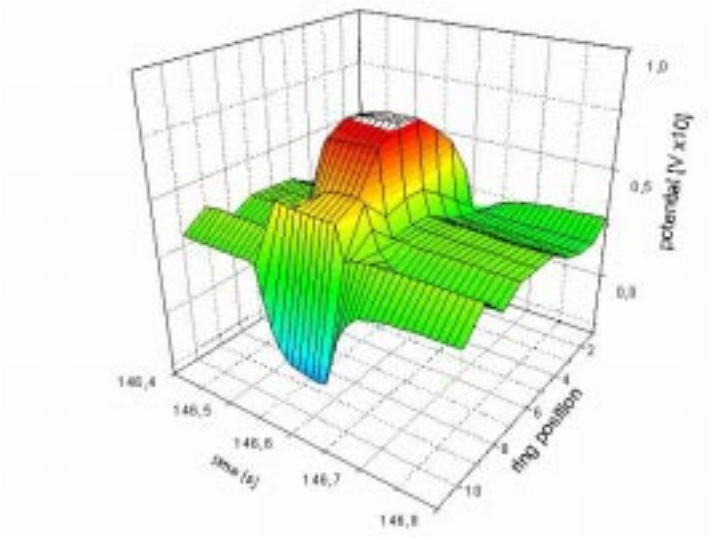

Figure 6-5: Temporal evolution of the local potential distribution in front of the WE during the application of a *positive* potential perturbation in the active state. The electrode numbering corresponds to the spatial position indicated in Figure 6-1. $U = 98mV$, other parameters as in the previous figure, probe 11 was inactive in this measurement.

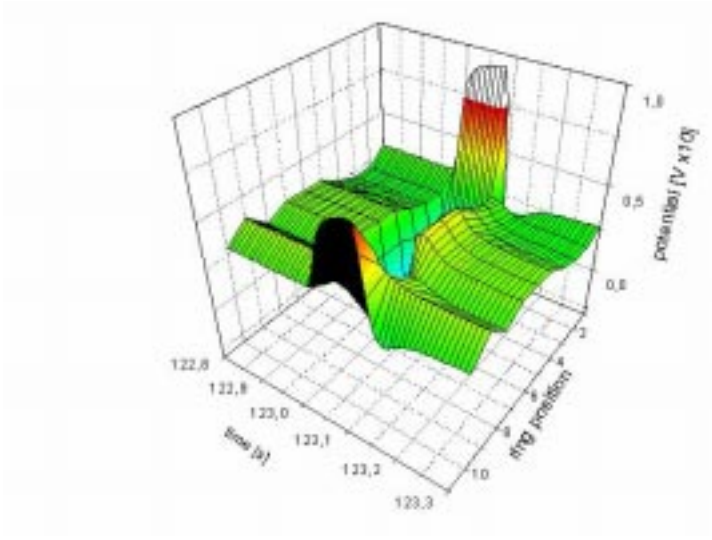

Figure 6-6: Temporal evolution of the local potential distribution in front of the WE during the application of a *negative* potential perturbation in the active state. $U = 98mV$, other parameters as in previous figure, probe 11 was inactive in this measurement.

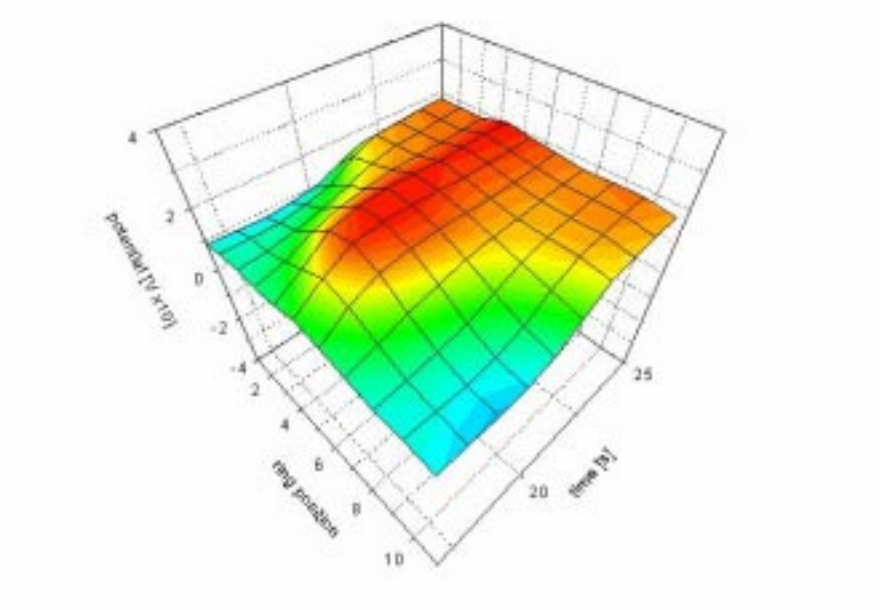

Figure 6-7: Spatiotemporal local potential distribution during a active-passive transition after spontaneous formation of a passive nucleus. $U = +290$ mV, 0,1 M HCOONa/ 0.05 M H_2SO_4 .

Fig. 6-7 such a spontaneous poisoning process was monitored using the multi-probe set-up.

After a slow anodic scan up to the maximum of Peak II, the scan was stopped. The system underwent a spontaneous current oscillation, followed by a slow decrease in the total current. Obviously, the spontaneous formation of a passive nucleus occurred near the ring position six which subsequently spread along the ring until the entire electrode was passivated. Interestingly, the front velocity (seen by the color-coded isopotential lines) was non-uniform; after a rapid initial spread, the front decelerates around $t = 20s$, before reaccelerating past $t = 21$ s immediately prior to the merging of both travelling fronts.

6.4.4 Travelling front patterns during the passive-active transition

Local triggering of potential fronts

Fig. 6-8 shows the dynamical response of the electrochemical system upon application of an overcritical positive, i.e. activating, perturbation. The potential ϕ_1, representing the local potential near the origin of the activation, drops first, followed by the activation of the opposite electrode side (ϕ_2). Simultaneously, the total current I non-uniformly, exhibiting a sharp rise when the electrode reaches complete activation.

The most straight-forward interpretation for this considerable delay between ϕ_1

and ϕ_2 is the time it takes for the active domain to spread around the entire ring. This is evidenced by the corresponding multi-probe measurement given in Fig. 6-9 and 6-10. There, one clearly distinguishes an active domain (low local potential) spreading gradually away from the location of the perturbation until the entire electrode has become active. Similar to findings during active-passive transitions, the front velocity is non-uniform, following the pattern fast-slow-fast.

Since the initial active domain is triggered where the perturbation was applied, this front creation will be referred to as "local triggering". Local triggering is the front creation mechanism usually observed in bistable chemical reaction -diffusion systems (RDS). From Fig. 6-8 and 6-9 the average front velocity of the triggered front is estimated to range between 3 and 30 cm/s depending on the detailed experimental conditions.

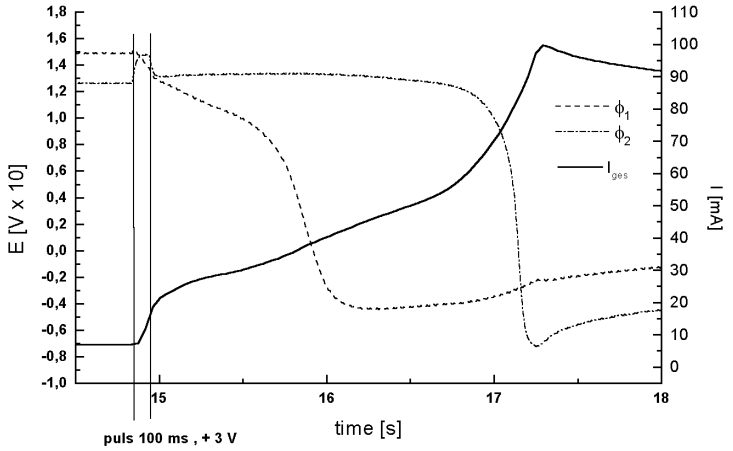

Figure 6-8: Time-trace of ϕ_1, ϕ_2 and I during a passive-active transition (**local triggering**). U = +423 mV, 0,1 M HCOONa/ 0,05 M H_2SO_4, $R = 0\Omega$, U_{pulse} = $+3V$, $100ms$

Remote triggering of fronts

In the following experiments, the sign of the local potential perturbation was inverted turning a locally activating perturbation into a locally passivating one. Since the system was prepared in the passive state, no response should usually be expected. Surprisingly, however, the measurements in Fig. 6-11 indicates that upon perturbation the local potential ϕ_2 drops sharply, followed by the delayed activation of ϕ_1. That travelling potential fronts are in fact involved in the dynamical response, is again evidenced by the corresponding multi-probe measurements displayed in Fig. 6-12 and 6-13 [190]. While the local interfacial potential near the pulse electrode increases, the electrode near position 5/6, i.e. on the opposite side of the pulse electrode becomes

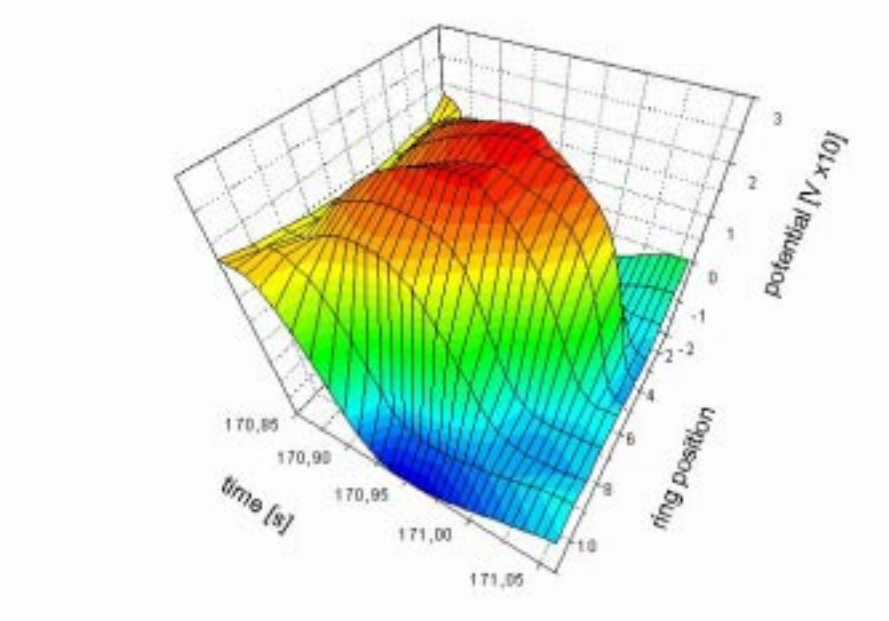

Figure 6-9: Potential distribution during a passive-active transition (**local triggering**). U = +320 mV, 0,1 M HCOONa/ 0,05 M H_2SO_4, $R = 0\Omega$, $U_{pulse} = +3V$, $100ms$

activated, followed by an active domain spreading around the WE. Since the overcritical perturbation created an activated domain at a remote location, this front creation mechanism will henceforth be referred to "remote triggering". Remote triggering is a qualitatively new type of phenomena unknown in chemical reaction-diffusion-media and has not been described in the literature sofar. The average front velocity in Fig. 6-11 and 6-12 is estimated to around 7 -20 cm/s.

The effect of an external ohmic resistance

From various studies on nonlinear electrochemical systems, it is known that the introduction of an external resistance in series to the electrochemical cell may considerably change the systems dynamics [65, 73, 153, 37, 38, 39, 189]. Here, the experimental effect of an external resistance on the spatial front triggering process was investigated.

Fig. 6-14 reports a typical dynamical response of the local potential distribution during a triggered passive-active transition in the presence of an ohmic resistance. During the perturbation ($t = 11,7 - 11,8\ s$), the change in the local potential was much smaller than in the absence of an resistance. More importantly, no creation of a local active domain could be observed. Instead, a homogeneous transition to the active state occurred. Obviously, an external resistance increases the spatial synchronization along the electrode suppressing the formation of inhomogeneous patterns.

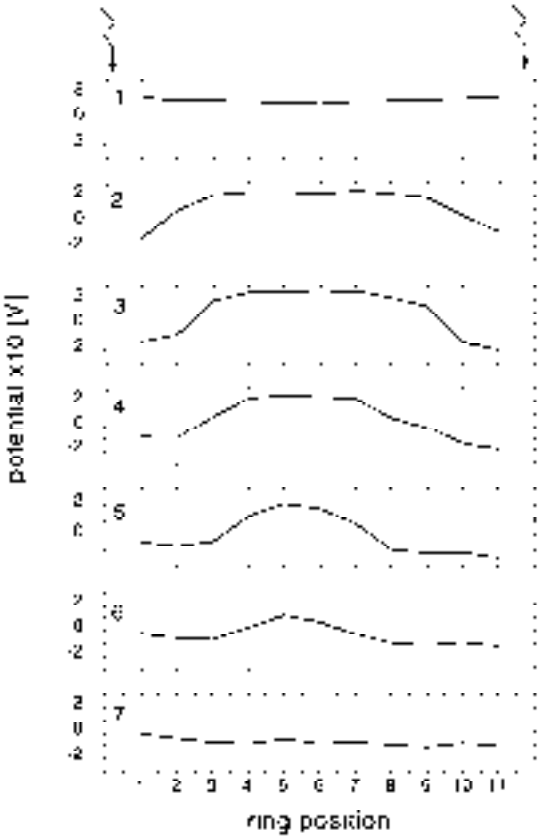

Figure 6-10: Temporal sequence (1-7) of instantaneous spatial potential profiles during the locally triggered transition of Fig. 6-9 . The time interval between two successive profile is 33 ms. The trigger pulse was applied immediately after time instant 1. The two arrows at position 0 (=12) indicate the location of the pulse electrode.

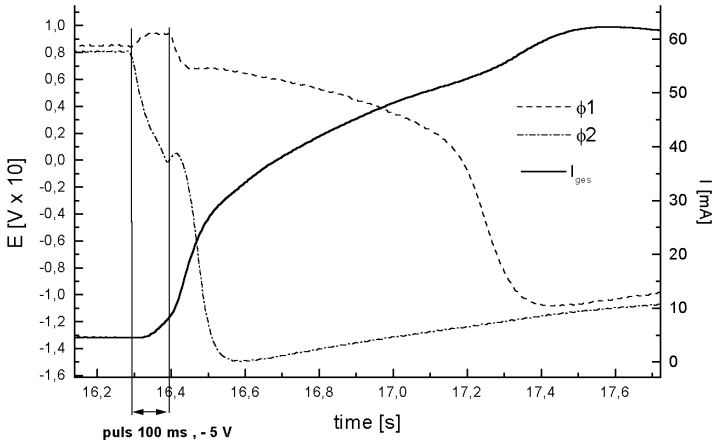

Figure 6-11: Time-trace of ϕ_1, ϕ_2 and I during a passive-active transition (**remote triggering**). $U = +335$ mV, 0,1 M HCOONa/ 0,05 M H_2SO_4, $R = 0\Omega$, $U_{pulse} = -5$ V, $100ms$

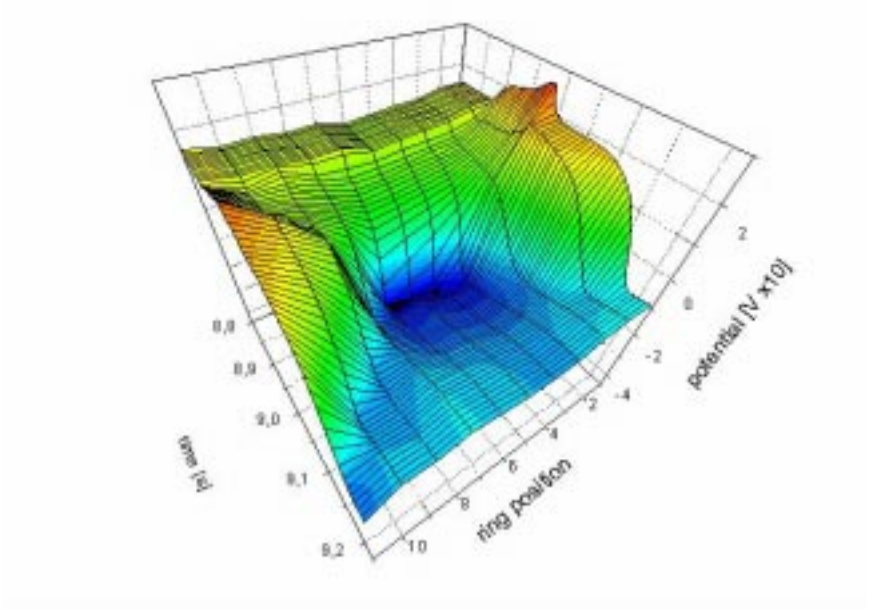

Figure 6-12: Potential distribution during a passive-active transition (**remote triggering**). $U = +300$ mV, 0,1 M HCOONa/ 0,05 M H_2SO_4, $R = 0\Omega$, $U_{pulse} = -5V$, $100ms$

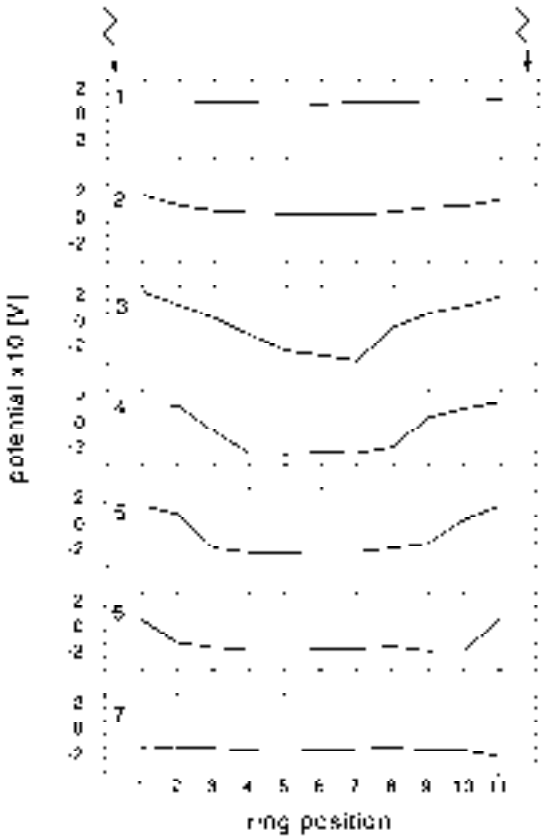

Figure 6-13: Temporal sequence (1-7) of instantaneous spatial potential profiles during the remotely triggered transition of Fig. 6-12. The time interval between two successive profile is 56 ms. The trigger pulse was applied immediately after time instant 1. The two arrows at position 0 (=12) indicate the location of the pulse electrode.

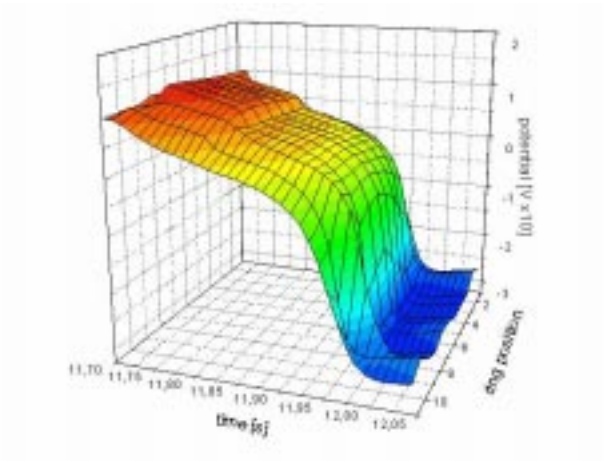

Figure 6-14: Potential distribution during a passive-active transition in the presence of an ohmic external resistance. $U = +239\ mV$,$\mathrm{U}_{pulse} = +10$ V, $R = 10\ \Omega$.

6.4.5 Spatiotemporally oscillating patterns

In the following series of experiments, the outer potential U was initially set at low values, followed by a slow anodic scan into the potential range where spontaneous oscillations occurred. Fig. 6-15 presents the time evolution of the local potential distribution recorded along the WE in the oscillatory regime. It is evident that the overall oscillatory behavior in the current is associated with a complex spatiotemporally oscillating pattern of the local potential. The potential distribution along one half of the WE ring is shifted by 180° relative to the other half of the electrode. The potential probe 6 appears to be nearly stationary. Fig. 6-16 is a blow-up of the previous figure and presents the instantaneous, spatially shifted potential distribution in more detail.

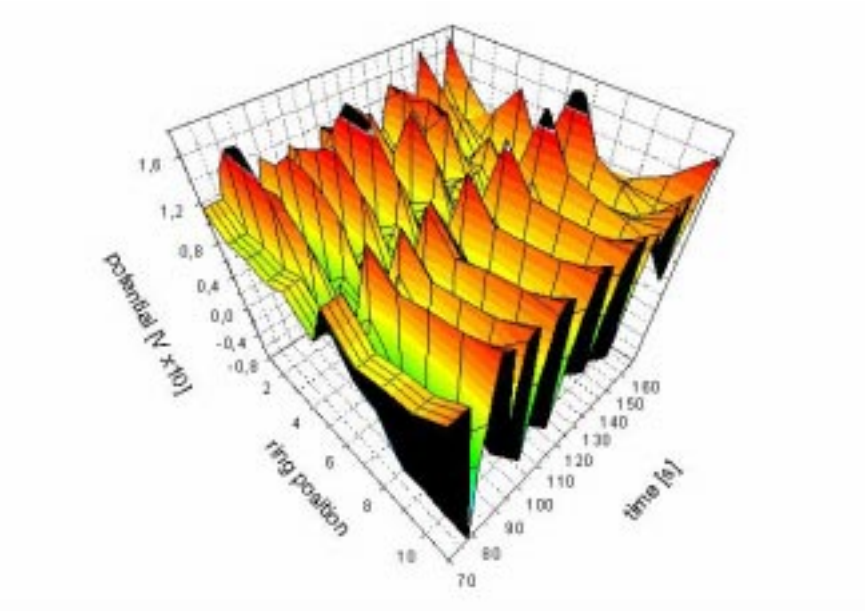

Figure 6-15: Spatiotemporal evolution of the local potential in front of the WE under oscillatory conditions. The potential distribution displays a **standing wave pattern.** $U = 325\ mV, 0.05$ M HCOONa/ 0.025 M H_2SO_4, no stirring, the oscillations have been induced by a homogeneous 200 ms/+200 mV pulse on the WE.

Fig. 6-17 refers to the measurement of Fig. 6-15 displaying the local time series of the oscillatory total current I_{tot} (upper graph), the local potential at probe 6 as well as at the opposite probes 2 and 8 (lower graph). As conjectured from Fig. 6-15, the oscillatory amplitude at point 6 is considerably smaller compared to probes 2 and 8 indicating a rather negligible superposition of a homogeneous oscillatory mode. The potential distribution therefore resembles strongly so-called anti-phase oscillations (standing wave pattern) with two points nearly at rest under periodic boundary conditions. While one node is visible at probe 6, the other node is necessarily lo-

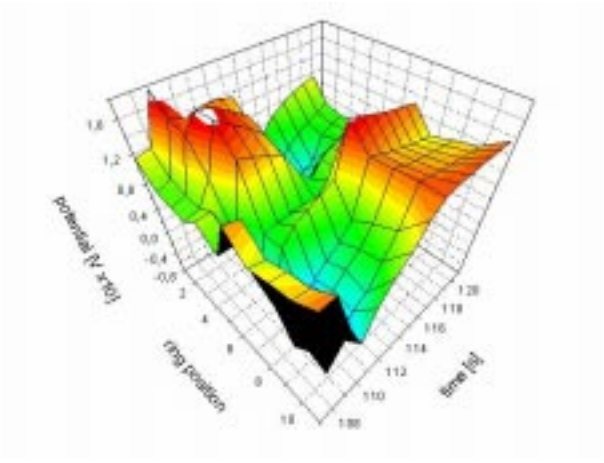

Figure 6-16: Blow-up of the standing wave pattern in the local electrode potential given in the previous Figure.

cated outside the spatial region monitored by the potential probe array, i.e. near the position 12 (pulse electrode).

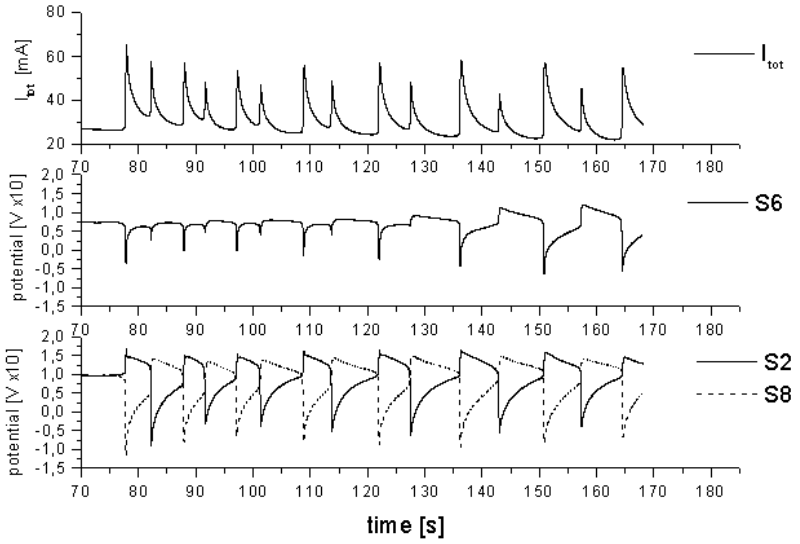

Figure 6-17: Local time series of the total current and local potentials at positions 6, 2 and 8 of the measurement given in Fig. 6-15.

Furthermore, Fig. 6-18 and 6-19 give a detailed account on the various instanta-

neous spatial profiles at various times (indicated by the letters A through H) during an oscillatory double cycle ($107s < t < 121s$) of Fig. 6-15. At peak values of I_{tot} (profiles A and E) the spatial inhomogeneity of the local potential is maximized, while for decreasing I_{tot} the potential distribution becomes more uniform at a relatively high potential level (profiles D and H). Probe 6 is clearly seen to be a node-like point. From Fig. 6-19 it also follows that the second interface outside the monitored region must have a steeper profile compared to that seen near probe 6.

Finally, the dependence of the shape of the space-time oscillations with respect to variations in the electrolyte solution was investigated. Fig. 6-20 displays an aperiodic time trace of the total current at a low electrolyte concentration characterized by an irregular current amplitude and period. The corresponding spatiotemporal local potential distributions are given in Fig. 6-21 and 6-22. There, one recognizes highly irregular spatiotemporal potential dynamics with the instantaneous anti-phase behavior along the ring electrode still distinguishable. Interestingly, the spatial location of the nodes of the aperiodic modes is now seen to be shifting which allows the observation of both nodes ($t = 67s$, $105s$).

It is obvious from Fig. 6-17 and Fig. 6-19 that the presented measurements are subject to a certain amount of modulation by noise and drifts, respectively. Still, the inhomogeneity of oscillatory patterns is sufficiently marked in order to exclude dynamical artifacts.

The effect of an external resistance

As described in chapter 4 and 5, an additional external resistance may greatly enlarge a system's parameter range of sustained current oscillations. When temporal oscillations are concerned, chapter 4 demonstrated in particular that an external resistance is essentially equivalent to increasing the solution resistance. Here, the influence of an external resistance on spatial oscillatory patterns is concerned.

Fig. 6-23 presents the typical time evolution of the local potential during current oscillations in the presence of an external resistance R. It is evident that the current oscillations were associated with a homogeneous potential distribution, while inhomogeneous patterns were absent. Thus, the external resistance induces a strong spatial coherence among distant locations along the WE indicating a stronger spatial coupling across the electrolyte.

6.4.6 Galvanostatic potential oscillations

A series of experiments was performed in order to check for inhomogeneous potential patterns under galvanostatic control. Fig. 6-24 shows a representative time series measured with the two-probe set-up.

Either local potential was perfectly in phase with the total oscillating potential of the WE, E_{WE}. No spatially inhomogeneous regime was observed at any time.

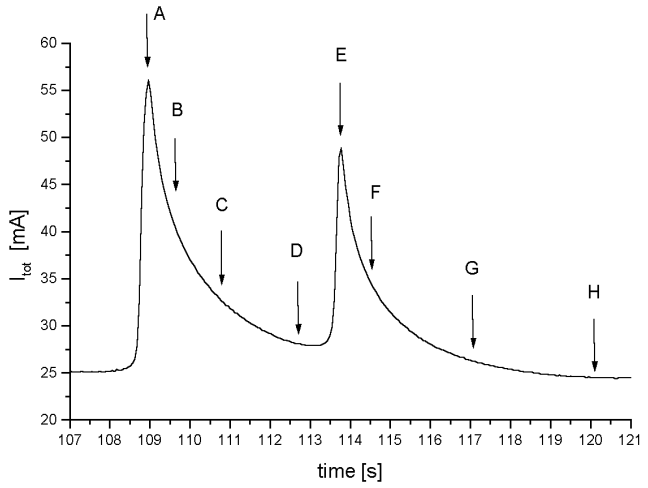

Figure 6-18: Blow-up of an oscillatory double cycle in I_{tot} from Fig. 6-15. The letters indicate 8 time instances for which the spatial profiles are given in the following figure.

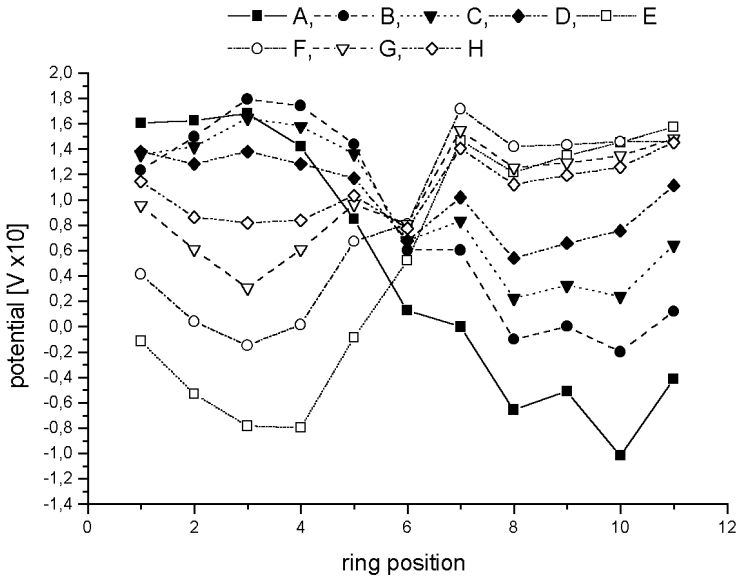

Figure 6-19: Spatial potential profiles at subsequent time instances A through H specified in the previous figure.

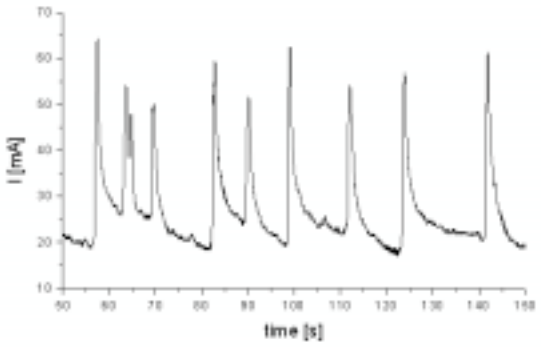

Figure 6-20: Aperiodic time-series of the total current I during formic acid oxidation at low electrolyte concentrations. U = 282 mV, 0,025 M HCOONa / 0,0125 M H_2SO_4, no stirring.

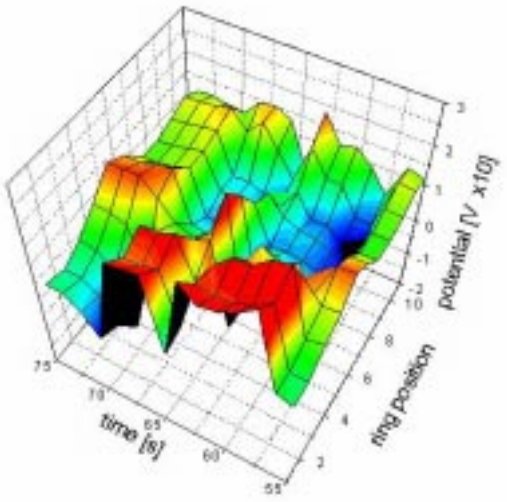

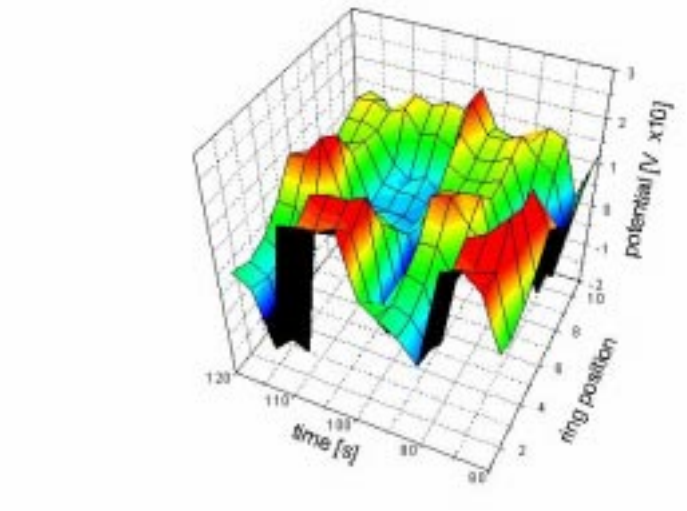

Figure 6-22: Local potential distribution at the electrode corresponding to the measurement given in Fig. 6-20.

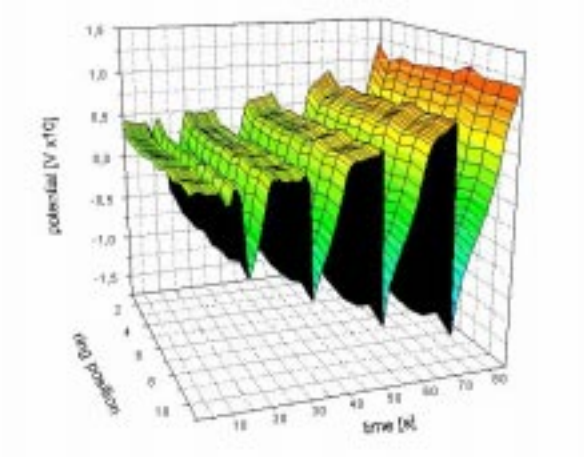

Figure 6-23: Potential distribution during current oscillations in the presence of an external resistance $R = 10\Omega$. $U = 396\ mV$, 0.1 M HCOONa/ 0,05 M H_2SO_4.

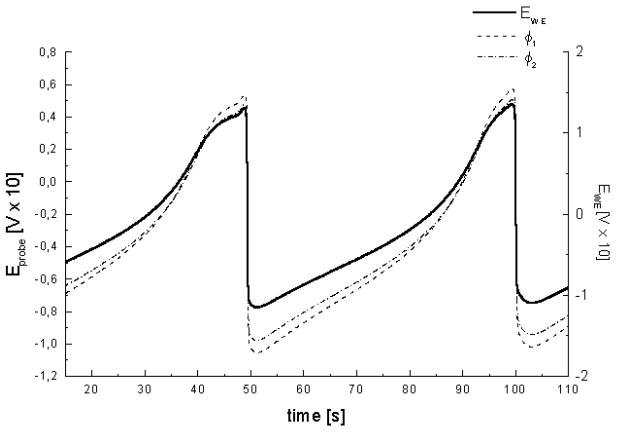

Figure 6-24: Galvanostatic time trace of the interfacial potential E_{WE} and of the two local potentials ϕ_1 and ϕ_2. $I = 18$ mA, 0,1 M HCOONa, 0,05 M H_2SO_4.

to the interplay of nonlinear chemical reaction processes and spatial electrochemical coupling. It will be argued that the aesthetics of the patterns are not an end in itself, instead they provide valuable insight in the nature of the spatial coupling mechanisms governing an electrochemical interface under the operative conditions.

6.5.1 Spatial coupling and patterns under bistable conditions

The present study examined both reactive fronts invading regions deactivated by oxygen-containing surface poisons (passive-active), and vice versa poisoning fronts invading reactive regions (active-passive). Propagation of fronts generally requires a positive spatial coupling on short ranges. Locally triggered fronts, i.e. fronts which arise near the location where a perturbation was applied as shown in Fig. 6-9 are the typical type of fronts described in literature.

While in electrodissolution systems front propagation phenomena can be traced back to the turn of the century [14], their first in-depth study in electrocatalytic systems was recently undertaken by Flätgen et al. [36, 35, 84, 85, 86]: The authors investigated dynamical front patterns on a Ag ring electrode in the bistable region of the $S_2O_8^{2-}$ reduction system with the RE being placed far away (several ring diameters) from the WE. They observed locally triggered fronts which accelerated during the transition.

In this study, the average front velocities of travelling domains depended upon whether an active-passive or passive-active transition was concerned. While active-passive transition led to very slow fronts (on the order of 10mm/s), front velocities associated with passive-active transitions showed a similar order of magnitude (30 - 300 mm/s) compared to those observed by Flätgen et al. In contrast to findings by Flätgen et al., fronts were observed to decelerate in the present electrochemical arrangement. Recently, Grauel et al. [189] found potential fronts during the $S_2O_8^{2-}$ reduction even to become stationary under a geometry similar to the one employed here, i.e. the RE was in the center of the WE. This strongly suggests the geometry to be responsible for the observed front effects rather than differences in the chemistry or electrode materials of the investigated processes. In fact, Grauel et al. argued that placing a RE close to the WE adds a negative global contribution to the positive nonlocal coupling which counteracts the front movement.

Here, first direct evidence of a negative electrochemical coupling across the electrolyte has been provided by the phenomenon of "remote triggering" of travelling potential fronts (Fig. 6-12) [190]: an additional passivation on one side of the already passive interface induced an almost immediate activation on the other. This surprising effect is obviously caused by the coupling through the electrical field across the electrolyte; "remote triggering" also definitely rules out chemical diffusion as the dominating coupling mechanism in electrochemical systems, in favor of a coupling mediated by migration currents.

Thus the present experiments suggest for the spatial electrochemical coupling to exhibit a positive sign on short ranges (propagation, "local triggering"), but a negative sign on long ranges ("remote triggering") under the employed geometry. The dependence of the coupling strength on distance with the coupling strength being finite at remote locations is generally referred to as nonlocality and has been accepted as a characteristic feature of the coupling in electrochemical systems [27].

The geometry-dependence of the spatial electrochemical coupling was thoroughly examined theoretically by Mazouz et al. [37, 38, 39]. Building on a model developed in ref. [84], they showed that the range of electrochemical migration coupling is a pure function of geometry, while its strength is associated with the solution con-

ductivity. Increasing the distance between WE and RE relative to the size of the WE, they argued, increases the range of the positive migration coupling leading to accelerating fronts. Using the same two-dimensional cylindrical model, Grauel et al. [189] extended its validity to electrode geometries where the RE is in the center of the WE. The authors assumed an averaging effect of the RE with respect to the WE potential which lead to a negative global contribution in the overall spatial coupling of the model accounting for the experimental observations.

Christoph [40, 190] elaborated on the original model for electrochemical pattern formation [84] such that far more complicated geometries in three-dimensional space became numerically tractable. He succeeded in presenting a consistent integral formalism (see chapter 2) which describes the spatial migration coupling for any geometry including the geometrical arrangement considered here. At the heart of his integral formalism lies a coupling function representing the range and sign of the spatial migration coupling along the electrode. As described in chapter 2, for large aspect ratios the coupling is a nonlocal positive one, while for small aspect ratios (RE in the center of the WE) a negative offset is superimposed. Thus, Christoph's theoretical predictions agree favorably with the present experimental findings.

In particular, numerical calculations using the one-variable potential model (pure bistable dynamics) nicely reproduce the experimental "remote triggering" phenomena as displayed in Fig.6-25: at $t = 0$, a passivating perturbation is applied near position $x = 0$ resulting in an activation of the electrode at the opposite side of the ring ($x = L/2$). When the propagating double front merges, the location near the origin of the perturbation activates $\phi(x = 0)$. The calculated current profile accompanying the front dynamics is also shown. The comparison of the calculations with the experimental findings of Fig.6-6 reveals a remarkable agreement. Calculated detailed space-time plots of both the locally and the remotely triggered transition are given in Fig.6-26 and Fig.6-27 which compare favorably with the measurements of Fig. 6-9 and 6-12.

As an external ohmic resistance is applied, the theoretical formalism predicts the superposition of a global positive coupling, shifting the overall coupling function upward in Fig. 2-6. Thus, past some critical value of the external resistance the positive global contribution overcompensates the negative global contribution by the geometry making "remote triggering" effects impossible and favoring homogeneous transitions rather than front propagation. The measurement in Fig. 6-14 verifies these theoretical predictions.

6.5.2 The oscillatory regime

Measurements of the local potential distribution during potentiostatic current oscillations revealed the formation of intriguing spatiotemporally oscillating patterns (antiphase oscillations, standing wave patterns). It is the first time such a self-organized standing structure was observed during an electrocatalytic reaction process. It is evident from the phase-shift in Fig. 6-16 that a long-range negative coupling must be operating along the ring electrode.

Previous reports on space-time oscillations involved exclusively electrodissolution

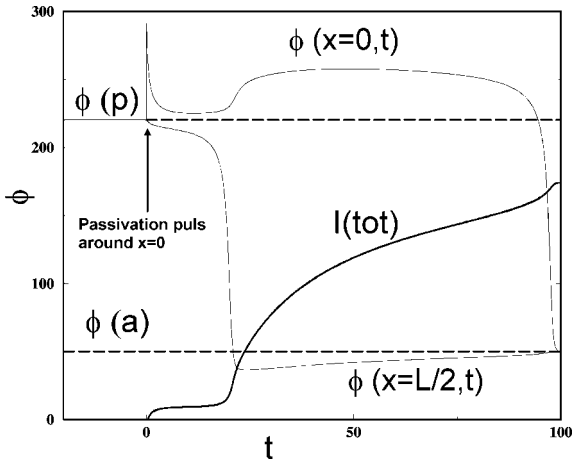

Figure 6-25: Numerical simulation of the "remote triggering" effect in a dimensionless one-variable reaction-migration model of ϕ according to [40]; x denotes the spatial coordinate, L is the electrode length, $\phi(a)$ and $\phi(p)$ denote the two coexisting stationary active and passive interfacial potential, respectively. Two time traces $\phi(x = 0), \phi(x = L/2)$ show the evolution of the local potential on opposite sides of the electrode. I denotes the total current during the transition.

reaction of metals such as Ni [34, 82, 191]or Co [87, 185, 186] in acidic media apart from catalytic surface reactions involving a gas-phase [192, 52, 57, 193]. However, the Ni dissolution system displayed antiphase oscillations only under galvanostatic conditions, i.e. in the presence of an additional integral constraint, while under potentiostatic control (with small external R) the observed patterns included propagating pulses and complex transients [82]. Unfortunately, the measurement of the local potential distribution under galvanostatic control was performed with respect to the RE leaving the influence of homogeneous potential oscillations on the instantaneous distribution unconsidered. Unlike those found during the formic acid oxidation, the patterns observed during Co dissolution included both antiphase oscillations and propagating pulses [194]. It is still unaccounted for under which conditions an oscillatory electrochemical process exhibits space-time oscillations or propagating pulses.

Standing wave patterns on isothermal catalysts were recently addressed theoretically by Krömker [195, 196, 55]. Krömker showed that in addition to an oscillating two-variable system a third fast-diffusive species is necessary in order to induce standing reaction wave patterns through a so-called wave bifurcation. The finite diffusion constant of the third species introduces an intrinsic spatial length scale of the RDS. Numerical simulation showed that through a wave bifurcation (secondary Turing bifurcation [54]) a stationary state loses stability and a standing, temporally oscillating wave forms.

The experimental study in the oscillatory regime was stimulated by theoretical consideration concerning reaction-migration systems performed by Christoph [40].

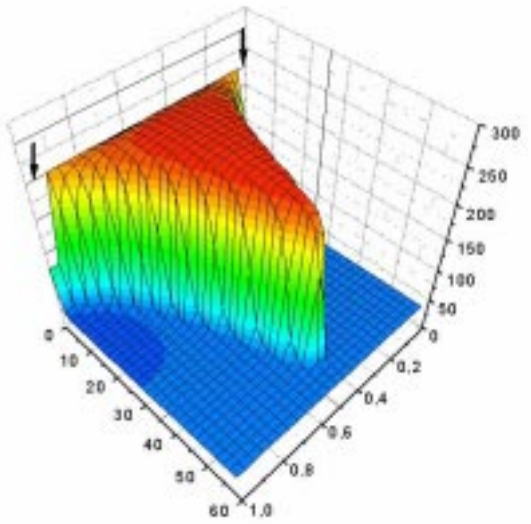

Figure 6-26: Simulated passive-active transition with a one-variable reaction-migration model in the bistable regime applying periodic boundary conditions: Local triggering. All quantities are given in dimensionless units. The passive and active state correspond to a potential of 230 and 30. A finite perturbation was applied in the region $0 = 2\pi$.

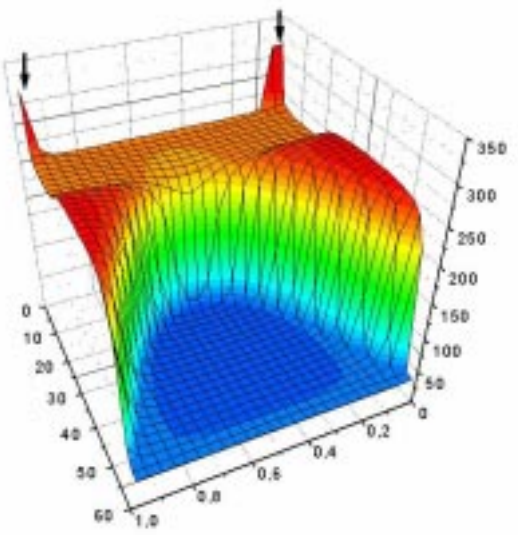

Figure 6-27: Simulated passive-active transition: Remote triggering upon local increase of the potential. Model and other parameters as in previous figure.

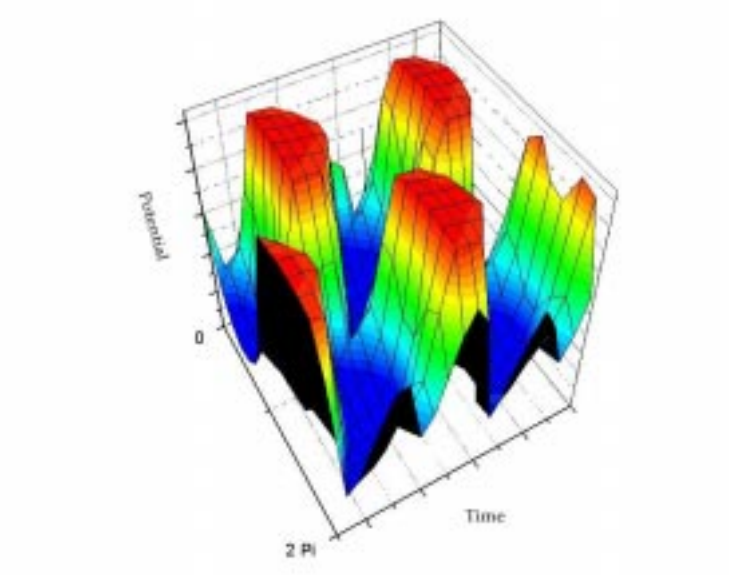

Figure 6-28: Calculated distribution of the interfacial potential in a two-variable reaction-migration model according to [40] in the oscillatory regime: Standing wave.

His integral formalism (chapter 2) helped establishing a consistent picture as to the origin of the electrochemical space-time oscillations under the geometry chosen. Upon adding a second variable to eq. 2-14 describing the time evolution of a slow chemical species, Christoph's formalism allowed for the investigation of spatiotemporal patterns under oscillatory conditions in dependence of system parameters such as the conductivity and the outer potential. Apart from propagating wave solutions, the model exhibited standing wave patterns (no homogeneous oscillation involved) as displayed in Fig. 6-28 in various parameter regions which show remarkable agreement with the experimental results in Fig. 6-15. Again, the negative long-range migration coupling is crucial for the observed sustained space-time dynamics.

Interestingly, one can establish a close link between the three-variable formalism used for standing wave phenomena in RDS and the two-variable reaction migration formalism. Upon setting the diffusion constant of the third variable of the RDS formalism to infinity (thereby losing the intrinsic wave length of that species) and subsequent adiabatic elimination of this variable, the dynamics of the RDS resembles that of the two-variable reaction-migration-system (RMS). This is due to the immediate effect of the eliminated variable just like the immediate effect of the electrical coupling across the electrolyte for the RMS. The missing of a finite intrinsic length scale leads to the stabilization of the inhomogeneous model of minimal wave number, i.e. the first mode, as observed in the present experiments: Doubling the ring size would again result in the formation of a standing wave with two nodes in contrast to a three-variable RDS where a standing structure with four nodes would result.

Similar to findings in the bistable regime, spatial inhomogeneities disappeared on

application of a sufficiently large external series resistance in favor of a homogeneous potential distribution along the WE. In analogy to the bistable case, the synchronization is due to a positive global coupling effect induced by the resistance which overcompensates the negative coupling based on the aspect ration of WE and RE.

6.6 Conclusions

Unusual front phenomena as well as complex spatiotemporally oscillating patterns manifested the nonlocal nature of the electrochemical spatial migration coupling its long-range effect being negative. The experimental findings compared favorably with theoretical model calculations.

However, apart from its contribution to a general understanding of spatial coupling mechanisms in physico-chemical systems, the present study is to also encourage to consider the possibility of performing surface electrocatalysis under coupling conditions where spatially inhomogeneous regimes are possible.

Similar to considerations made for temporally oscillating chemical systems [197, 198], it is conceivable that conditions of spatiotemporal patterns may bring along advantages with respect to chemical yield, efficiency or robustness towards perturbations. The latter shall be illustrated as follows. Consider an electrochemical process at an active ring electrode under the electrode geometry used above, i.e. in the presence of a negative long-range coupling. Now suppose that some portion of the active electrode becomes deactivated due to some surface poison. The local interfacial potential will rise at that point, at the same time lowering the interface potential on the opposite side. The latter, in turn, will presumably nearly restore the previous overall rate, in contrast to conditions where the long-range negative coupling is absent.